Bioactive Materials 17 (2022) 334–343

Contents lists available at ScienceDirect

Bioactive Materials

journal homepage: www.keaipublishing.com/en/journals/bioactive-materials

Improved mechanical, degradation, and biological performances of Zn–Fe alloys as bioresorbable implants

Yingchao Su [a], Jiayin Fu [b,c], Wonsae Lee [a], Shaokang Du [d], Yi-Xian Qin [a], Yufeng Zheng [e], Yadong Wang [b], Donghui Zhu [a,*]

[a] Department of Biomedical Engineering, Stony Brook University, Stony Brook, NY, USA
[b] Nancy E. and Peter C. Meinig School of Biomedical Engineering, Cornell University, Ithaca, NY, USA
[c] Department of Cardiology, Sir Run Run Shaw Hospital, Zhejiang University, Hangzhou, Zhejiang, China
[d] Academy for Advanced Interdisciplinary Studies, Peking University, Beijing, China
[e] School of Materials Science and Engineering, Peking University, Beijing, China

ARTICLE INFO

Keywords:
Zinc
Mechanical
Degradation
Biocompatibility
Antibacterial

ABSTRACT

Zinc (Zn) is a promising bioresorbable implant material with more moderate degradation rate compared to magnesium (Mg) and iron (Fe). However, the low mechanical strength and localized degradation behavior of pure Zn limit its clinical applications. Alloying is one of the most effective ways to overcome these limitations. After screening the alloying element candidates regarding their potentials for improvement on the degradation and biocompatibility, we proposed Fe as the alloying element for Zn, and investigated the *in vitro* and *in vivo* performances of these alloys in both subcutaneous and femoral tissues. Results showed that the uniformly distributed secondary phase in Zn–Fe alloys significantly improved the mechanical property and facilitated uniform degradation, which thus enhanced their biocompatibility, especially the Zn-0.4Fe alloy. Moreover, these Zn–Fe alloys showed outstanding antibacterial property. Taken together, Zn–Fe alloys could be promising candidates as bioresorbable medical implants for various cardiovascular, wound closure, and orthopedic applications.

1. Introduction

Bioresorbable implants made of biodegradable materials are expected to temporarily support the injured tissue and then degrade without a secondary surgery after the tissue recovery [1]. When compared to the biodegradable polymers, biodegradable metals, *i.e.* magnesium (Mg), iron (Fe), and zinc (Zn), possess much higher mechanical strength and are suitable for the load bearing applications [2]. With moderate degradation rate and significant biological roles, Zn has been regarded as the most promising candidate in the cardiovascular [3–5] and orthopedic applications [6,7]. Nevertheless, the mechanical strength of pure Zn is still not enough for the load bearing applications [8,9]. Moreover, their mechanical integrity during the degradation process would be further deteriorated due to the localized degradation behavior of pure Zn implants [3–5].

Alloying is the most critical and effective way to address the issues related to mechanical and corrosion properties for metallic materials [1,10]. The selection of alloying elements is important in order to improve these properties while not compromising the biocompatibility. As an essential element in human body, Mg can not only act as a metallic substrate but also be an alloying element in Zn alloys. Zn–Mg alloys have been vastly studied in the past few years [6,11–14]. As another biodegradable metal, Fe is also an essential element required for blood production and a wide variety of metabolic processes [15], but studies have been sporadic for Zn–Fe alloys. Electrodeposited Zn–Fe alloys have been explored as surface coatings for corrosion resistance [16,17]. As cast Zn–Fe alloys have also been implanted subcutaneously for evaluations of degradation rate and biocompatibility [18,19].

To study the effects of microstructure of Zn–Fe alloys, 0.4 and 2.5 wt % of Fe were chosen to obtain two different percentages of intermetallic phases based on a detailed previous study on the phase diagram in the Zn–Fe binary system [20]. It is known that the plastic deformation processing techniques could significantly improve the mechanical property of metals, including the mechanical strength and toughness

Peer review under responsibility of KeAi Communications Co., Ltd.
* Corresponding author.
E-mail address: Donghui.Zhu@stonybrook.edu (D. Zhu).

https://doi.org/10.1016/j.bioactmat.2021.12.030
Received 14 October 2021; Received in revised form 7 December 2021; Accepted 24 December 2021
Available online 30 December 2021

[21–23]. Therefore, in the present study, we further extruded Zn–Fe alloys to achieve sufficient mechanical properties for appropriate medical applications. Two *in vivo* models, subcutaneous and femoral implantations, were explored in rats. These two *in vivo* locations offer comprehensive assessments of the Zn alloy implants in both soft and hard tissues for biomedical applications, such as cardiovascular, wound closure, and orthopedic applications, respectively.

2. Materials and methods

2.1. Materials preparation and surface characteristics

Zn-0.4Fe and Zn-2.5Fe (w.t.%) alloys were prepared using pure Zn (99.99%) and pure Fe (99.99%) by gravity casting. The casted alloys were heat-treated at 350 °C for 48 h followed by water quenching and then extruded at 260 °C from Ø 28 mm cylinder to Ø 10 mm cylinder. Pure Zn were also extruded for comparison. All Zn materials were cut into cylinder discs (Ø 10 mm × 5 mm) for *in vitro* tests and wires (Ø 0.25 mm × 5 mm) for *in vivo* implantation. The disc samples were polished using #1200 sandpaper and the rod samples were electropolished using a voltage of 10 V in a mixture of ethanol (885 ml), butanol (100 ml), aluminum chloride hexahydrate ($AlCl_3{\cdot}6H_2O$) (109 g), zinc chloride ($ZnCl_2$) (250 g) and water (120 ml) for 2 min [24]. The microstructure and phase composition were tested by optical microscopy and X-ray powder diffraction (XRD), respectively.

2.2. Mechanical test

Mechanical property was measured at a strain rate of 1×10^{-4} s^{-1} using a universal material test machine (Instron 5969, USA). The specimens were machined to the desired dimensions according to ASTM-E8/E8M standards [25]. The yield strength was determined as the stress at which the 0.2% plastic deformation occurred.

2.3. In vitro degradation test

All the degradation tests were carried out in a modified Hanks' solution at 37 ± 0.5 °C as described previously [26–29]. Briefly, a Princeton Versa Stat 3 electrochemistry workstation was used to measure the electrochemical degradation behaviors. The electrochemical impedance spectroscopy (EIS) was tested in a frequency range of 10^{-2}–10^5 Hz with a potential amplitude of 10 mV. The potentiodynamic polarization test were performed at a scan rate of 1 mV/s. The corrosion rate (*CR*, mm/y) was calculated based on the electrochemical corrosion current density (i_{corr}, μA/cm^2) according to the following equation [28,30]:

$$CR_i = 3.27 \times 10^{-3} . \frac{i_{corr}}{\rho} EW$$

where ρ is the material density (g/cm^3) and *EW* is the corresponding equivalent weight (g).

The immersion degradation tests were performed for 1 and 3 months according to a previous study [27]. Briefly, the solution was refreshed every week due to the slow degradation of Zn materials. The pH values of the solution with different samples were monitored and were also measured during the immersion tests. The surface morphologies and phase composition of degraded samples after 1 and 3 months of immersion were tested with scanning electron microscopy (SEM) and XRD. The CR_W (mm/y) was calculated based on weight loss (W_{loss}, mg) according to the following equation [31]:

$$CR_W = 87.6 \times \frac{W_{loss}}{\rho A t}$$

where ρ is the material density (g/cm^3), t is immersion time (h), A is sample surface area (cm^2).

2.4. Hemocompatibility

The hemolysis tests and platelet adhesion tests were performed according to the method described previously [7,32]. In brief, healthy human blood (anticoagulant with 3.8% citric acid sodium, Zen-Bio, US) was diluted by 0.9% sodium chloride solution with a volume ratio of 4:5. All samples were pre-cultured with 9.8 ml 0.9% sodium chloride solution at 37 °C for 30 min and 0.2 mL diluted blood was then added to each tube and incubated at 37 °C for 60 min. Deionized water and 0.9% sodium chloride solution were incubated with 0.2 mL diluted blood as the positive and negative control, respectively. After centrifuging at 3000 rpm for 5 min, the supernatants were collected in 96-well plates and the absorbance (*A*) was measured by a plate reader (Cytation 5, Biotek, US) at 545 nm. The hemolysis rate (HR) was calculated by the following equation:

$$\text{Hemolysis} = (A_{sample} - A_{negative})/(A_{positive} - A_{negative})$$

Platelet rich plasma (PRP) with 10^8/μl platelets (Zen-Bio, US) was used for platelet adhesion test. 50 μl PRP was overlaid on each sample surface and incubated at 37 °C for 1 h. After gently rinsed by PBS for 3 times to remove the non-adherent platelets, adherent platelets on samples were fixed with 4% paraformaldehyde (PFA, Affymetrix, US) and 2% glutaraldehyde solution (Fisher Chemical, US) at room temperature for 2 h, then dehydrated with gradient alcohol solution (30%, 50%, 70%, 90%, and 100%) and hexamethyldisilazane (HMDS) for 10 min, respectively, and finally dried in desiccator. The samples were coated with gold and observed by SEM. The number of adherent platelets was counted on at least five different SEM images for each sample.

2.5. Cytocompatibility

Human endothelial cells (EA.hy926, ATCC CRL-2922, US) and human aortic vascular smooth muscle cells (HA-VSMCs, ATCC CRL-1999, US) were cultured in 75 cm^2 flask (BD Bioscience) with Dulbecco's Modified Eagle Medium (DMEM, ATCC, US) containing 10% fetal bovine serum (FBS, ScienCell) and 1% penicillin/streptomycin solution (P/S, ScienCell) [33–35]. For the indirect assays, extract media was prepared by incubating samples in the corresponding cell culture media at a ratio of 1.25 cm^2/mL for 3 days. Afterward, the collected extract solution was diluted with culture media to specific concentrations of 25%. The cell viability was measured with the MTT assay (Thermo Fisher Scientific, US) after cultured with the extract solution for 1, 3, and 5 days [36,37]. Cells with a density of 1×10^5/well were seeded onto different samples with and without being precultured in DMEM for 3 days in a 24 well plate. After 3 days of cell culture, the cell morphology was observed by SEM after being fixed and dehydration in the same method with the platelet adhesion test as described above.

2.6. Antibacterial property

Escherichia coli (*E. coli*, ATCC 25922, US) and *Staphylococcus aureus* (*S. aureus*, ATCC 29213, US) were cultured according to the procedures in a previous study [38]. Briefly, the bacteria were cultured in Tryptic Soy Broth (TSB) media at 37 °C and 220 rpm to reach the optical density of 0.5–0.6 at 600 nm. The antibacterial performance was tested with the same procedures in our previous study [39]. 2 ml of the diluted bacterial suspension with a concentration of 5×10^5/mL in TSB media was incubated with samples for 24 h at 37 °C and 120 rpm. Diluted bacterial suspension without samples was used as negative control. The absorbance of the collected bacteria suspension was read at 600 nm. Antibacterial rates in the TSB media were calculated with the following equation: Antibacterial rates = $(A_{negative} - A_{sample})/A_{negative}$. Before the SEM imaging, samples were fixed and dehydrated with the same procedures as described above.

2.7. In vivo subcutaneous and femoral implantation

The animal protocols were approved by the Stony Brook University Institutional Animal Care and Use Committee (IACUC) and the Cornell University IACUC. Male young Sprague–Dawley (SD) rats (8–10 weeks, body weight = 300–325 g, Taconic Biosciences, NY) were used for subcutaneous and femoral implantation (n = 5 for each implant at each time point). Before the surgery, the rats were anesthetized, and the operation side was shaved and disinfected. Subcutaneous implantation was conducted as described in previous publications [7,40]. In brief, incisions were made down to the subcutaneous tissue of the back. A subcutaneous pocket was built in which the alloys were inserted. 4 incisions were made on the back of each rat. One wire implant (0.25 mm in diameter, 15 mm in length) was implanted in subcutaneous pocket through one incision. For the bone implantation, a 2 cm incision will be made along the lateral aspect of femur. A cylindrical hole (0.3 mm in diameter) was drilled in the femoral condyle perpendicular to the long axis of the right femur. Metallic wires (0.25 mm in diameter, 3 mm in length) were inserted into the cylindrical hole. The incision was closed in layers with sutures and left un-casted.

After 3 months of implantation, the rats were scanned with micro-CT and samples were harvested for SEM imaging and histological analysis including H&E, Masson trichrome, Goldner trichrome, Verhoeffe-Van Gieson, and CD11b and CD68 immunofluorescent staining [5]. Briefly, explanted specimens were rinsed in 0.1 mmol/l sodium phosphate buffer (pH 7.2 ± 0.1) and fixed in 4% PFA followed by embedding with paraffin and polymethylmethacrylate (PMMA) for subcutaneous (n = 5) and femoral tissue (n = 5), respectively. Embedded wire implant was cut and sectioned in to 4 μm thick slices perpendicular to the long axis of the wire implant. The subcutaneous tissue slices were stained with H&E, Masson trichrome, Verhoeffe-Van Gieson, and CD11b and CD68 immunofluorescent staining, while the femoral tissue slices were stained with Goldner trichrome and Verhoeffe-Van Gieson. After being polished, and gold coated, and the cross sections of the wire implants were observed with SEM imaging and EDS. The bone formation was quantified using ImageJ software based on the at least 5 cross-sectional SEM images. Bone-to-implant contact (BIC) is calculated through normalizing the implant perimeter directly in contact with bone over the implant perimeter length, while bone area (BA) represents the ratio of bone area to total area extending 100 μm from the implant [8]. The osteoid layer thickness was also measured surrounding the implants.

2.8. Statistical analysis

All data was presented as mean ± standard deviation. One-way ANOVA followed by Turkey's post-hoc test was used to analyze the statistical significance. Power analysis for ANOVA determined that each assay had at least three replicates and repeated 3 times independently to achieve 0.9 power for $\alpha = 0.05$. $P < 0.05$ was considered as statistically significant.

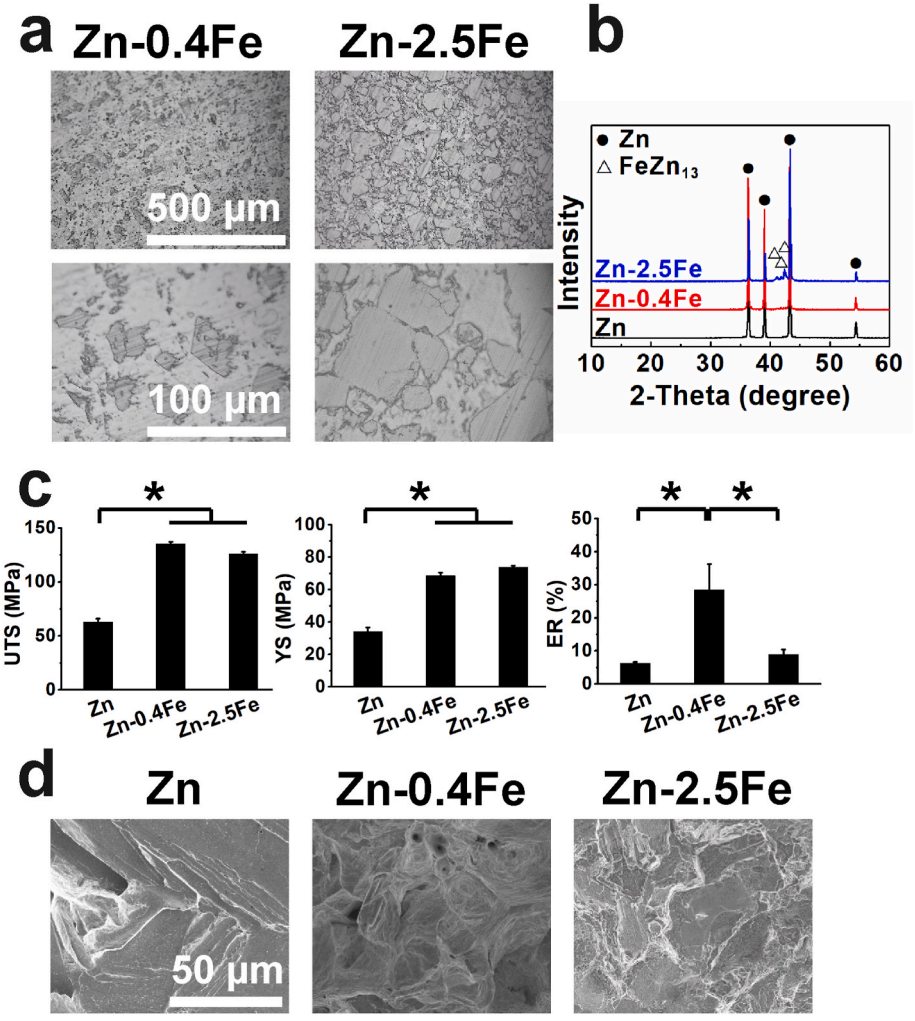

Fig. 1. Microstructures and mechanical behaviors of the as-extruded Zn–Fe alloys. (a) Microstructures, (b) XRD patterns, and (c) mechanical properties. UTS: Ultimate tensile strength, YS: yield strength, ER: elongation to failure. (d) fracture morphology after tensile test.

3. Results

3.1. Microstructure and mechanical property

After fabrication, the microstructure, XRD patterns, and mechanical property of the extruded Zn–Fe alloys were examined. The alloys showed an η-Zn phase and a uniformly distributed second phase (Fig. 1a), which is $FeZn_{15}$ as identified by the XRD patterns (Fig. 1b). The phases' percentages are different in the two alloys: the η-Zn and $FeZn_{13}$ phases are dominant in Zn-0.4Fe and Zn-2.5Fe alloys, respectively. The different microstructures affect the different mechanical properties of these two alloys, as shown in Fig. 1c. Both alloys showed significantly improved mechanical strengths, while the Zn-0.4Fe alloy had significantly higher elongations (~30%) than pure Zn (8%) and Zn-2.5Fe alloy (~10%). This means the Zn-0.4Fe alloy possessed the optimum combination of mechanical strength and ductility. The fracture morphology after tensile tests in Fig. 1d showed the deformation mode during the fracture process. The pure Zn exhibited a cleavage fracture morphology with cleavage planes, while the Zn-0.4Fe alloy showed dimple fracture morphology with river patterns. However, as the $FeZn_{15}$ increased, Zn-2.5Fe alloy showed a brittle fracture morphology with river patterns.

3.2. In vitro degradation behavior

The different microstructures of Zn and Zn–Fe alloys also have critical impacts on their degradation behaviors. The electrochemical corrosion tests were carried out to characterize the corrosion rate and corrosion resistances. All the polarization and EIS curves showed the similar trends (Fig. 2a and b), indicating the similar electrochemical corrosion reactions occurred in the tests. Compared to the pure Zn, Zn–Fe alloys possessed lower corrosion current density and corrosion rates (Fig. 2c), while the higher polarization resistances and total corrosion resistance from the EIS tests (Fig. 2c). In addition, the Zn-0.4Fe alloy exhibited a slightly higher corrosion resistance than the Zn-2.5Fe alloy.

The degradation behaviors were also characterized by the long-term immersion tests in the Hanks' solution (Fig. 3). The Zn showed a uniform degradation morphology up to one month but then turned into localized degradation with corrosion pitting during 3 months' immersion, consistent with previous studies [3–5]. The small amount of Fe addition changed the degradation pattern to more uniform degradation pattern. There were small pits uniformly distributed on its surface after one month and a thin film composed of corrosion products formed on the degraded surface after 3 months. However, as the amount of Fe in the alloy increased, the degradation pattern changed to severely localized degradation. There were much more degradation products formed around the degradation pits at one month and grew into localized thick films after 3 months. According to the XRD patterns (Fig. 3b), all the degradation products were similar and made of $Zn(OH)_2$ and $CaZn_2(PO_4)_2{\cdot}2H_2O$ after 1 month. Compared to the other two groups, there were less degradation products and no $Zn_3(PO_4)_2{\cdot}4H_2O$ on the Zn-0.4Zn surface during the 3 months of immersion test. All the samples showed similar corrosion rates and stable pH change during the 3 months of immersion (Fig. 3c and d). The corrosion rate of Zn-0.4Fe alloy was slightly lower than that of the other two groups, which is consistent to the electrochemical corrosion results.

3.3. In vitro cytocompatibility and hemocompatibility

Two different vascular cells and platelet were used to test the cytocompatibility and hemocompatibility of Zn and Zn–Fe alloys, as shown in Fig. 4. The endothelial cells showed good attachment and elongated morphology on all Zn materials (Fig. 4a), while the smooth muscle cells showed isolated and round morphology (Fig. 4b). The cell viabilities of these two cells with the material extracts were shown in Fig. 4d and e, respectively. Compared to the pure Zn, two Zn–Fe alloys showed higher cell viability for endothelial cells, whereas the Zn-0.4Fe alloy induced lower cell viability for smooth muscle cells.

Platelet adhesion and hemolysis tests were conducted to evaluate the hemocompatibility of Zn materials. There were a few adhered platelets dispersedly distributed on pure Zn and Zn-0.4Fe alloy surfaces with little spreading (Fig. 4c). More platelets on the Zn-2.5Fe alloy were activated than on the other two groups. The numbers of adhered platelets on all Zn surfaces were also similar on pure Zn and Zn-0.4Fe alloy, and slightly increased on Zn-2.5Fe alloy. Their hemolysis rates of the two alloys were lower than that of pure Zn, but all values were much below the hemolysis limit (5%), indicating their good hemocompatibility.

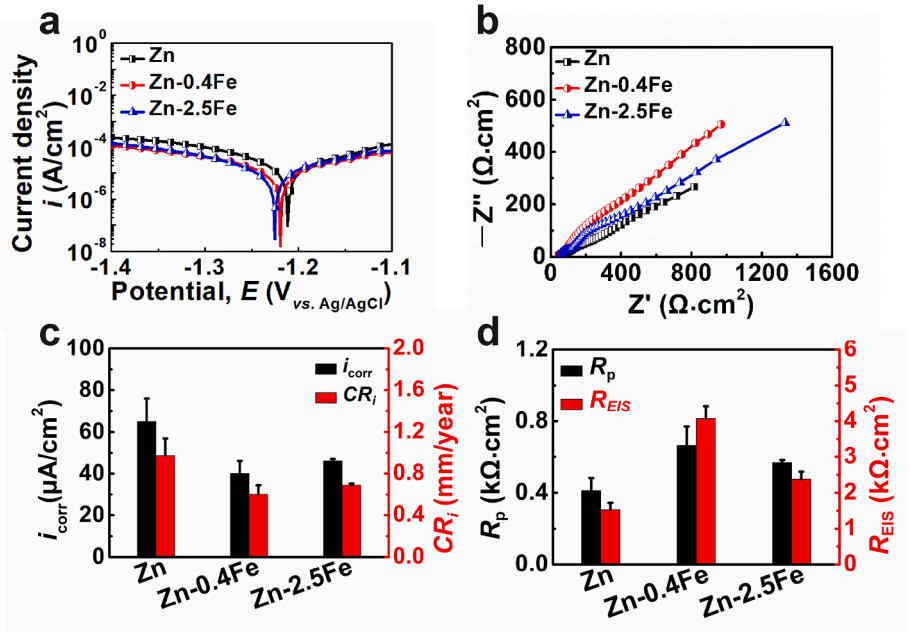

Fig. 2. Electrochemical corrosion behaviors of pure Zn and Zn–Fe alloys in Hank's solution. (a) potentiodynamic polarization, (b) Electrochemical impedance spectroscopy (EIS); (c) corrosion current density and corrosion rates (d) polarization resistance and total resistance from EIS data.

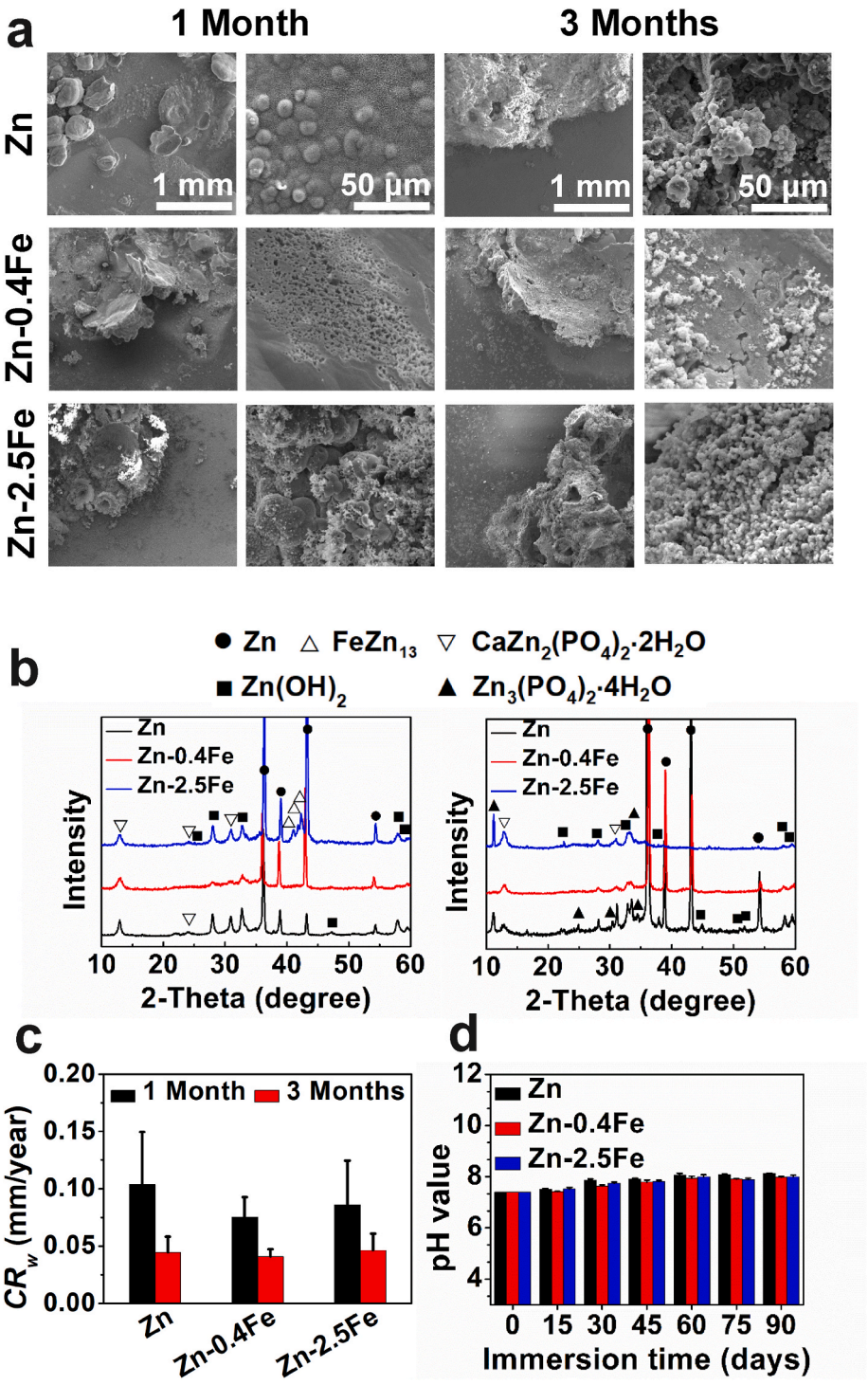

Fig. 3. Immersion degradation results of pure Zn and Zn–Fe alloys in Hank's solution for 1 and 3 months. (a) Degraded surface morphology, (b) XRD patterns, (c) corrosion rate, (d) evolution of pH values with immersion time.

3.4. Antibacterial property

The antibacterial property of Zn and Zn–Fe alloys was tested with *E. coli* and *S. aureus*, respectively, as shown in Fig. 5. There was a few bacterial adhesions and no biofilm formation on all Zn materials' surfaces. There were even some broken *E-coli* cells on these materials (Fig. 5a). Different with the isolated morphology of *E-coli*, *S. aureus* showed an interconnected morphology. There are no significant differences of antibacterial rates in the bacterial culture media for these materials. All Zn materials exhibited much higher antibacterial rate to the *S. aureus* than *E-coli* (Fig. 5b).

3.5. In vivo subcutaneous implantation

Zn and Zn–Fe alloys were implanted in soft tissues first, i.e., the rat subcutaneous tissue, to test the degradation behaviors and tissue responses (Fig. 6). It could be observed from macroscopic views and micro-CT scanning images that there were more degradation products aggregated surrounding both Zn–Fe alloy wire implants, and the Zn-2.5Fe wire implant was fractured with a much higher degradation rate

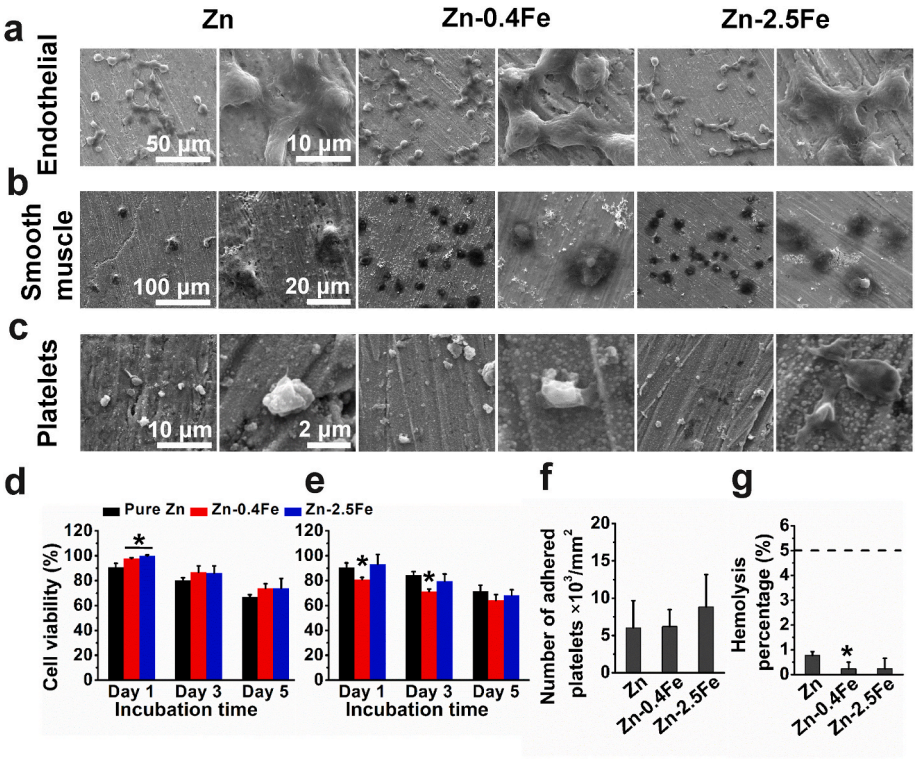

Fig. 4. Cytocompatibility and hemocompatibility of Zn and Zn–Fe alloys. Adhesion morphology of (a) endothelial cells, (b) smooth muscle cells, and (c) platelets, cell viability of (d) endothelial and (e) smooth muscle cells, (f) number of adhered platelets, and (g) hemolysis percentage. *$p < 0.05$, compared with pure Zn group.

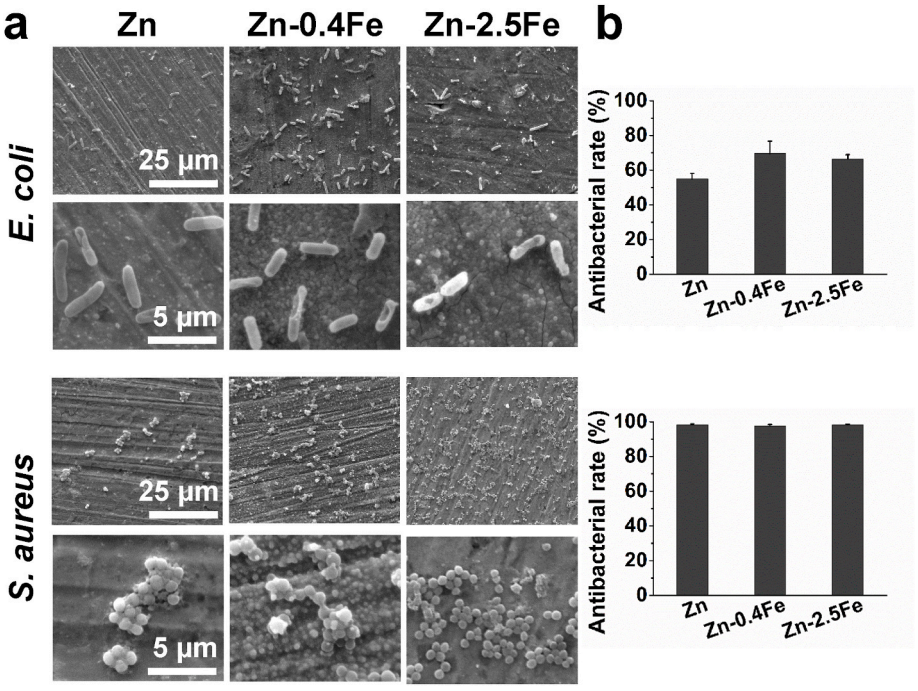

Fig. 5. Antibacterial performance of pure Zn and Zn–Fe alloys cultured with *E. coli* and *S. aureus* for 24 h. (a) SEM images of bacterial adhesion on sample surfaces. (b) Antibacterial rates in the medium.

than pure Zn wire implant (Fig. 6a–c). The histological staining showed there were fibrotic encapsulation surrounding all wire implants (Fig. 6d). The Masson and Verhoeff's staining also exhibited the formations of collagen and elastin with these Zn implants, respectively. The immunostaining with CD11b and CD68 shows the aggregation of monocytes/macrophages. After 3 months of implantation, there was little immune response to pure Zn wire implant. There were stronger immune responses to the Zn–Fe alloys, especially the Zn-2.5Fe alloys, which might be related to the massive degradation products formed at the interface between the implants and surrounding tissues.

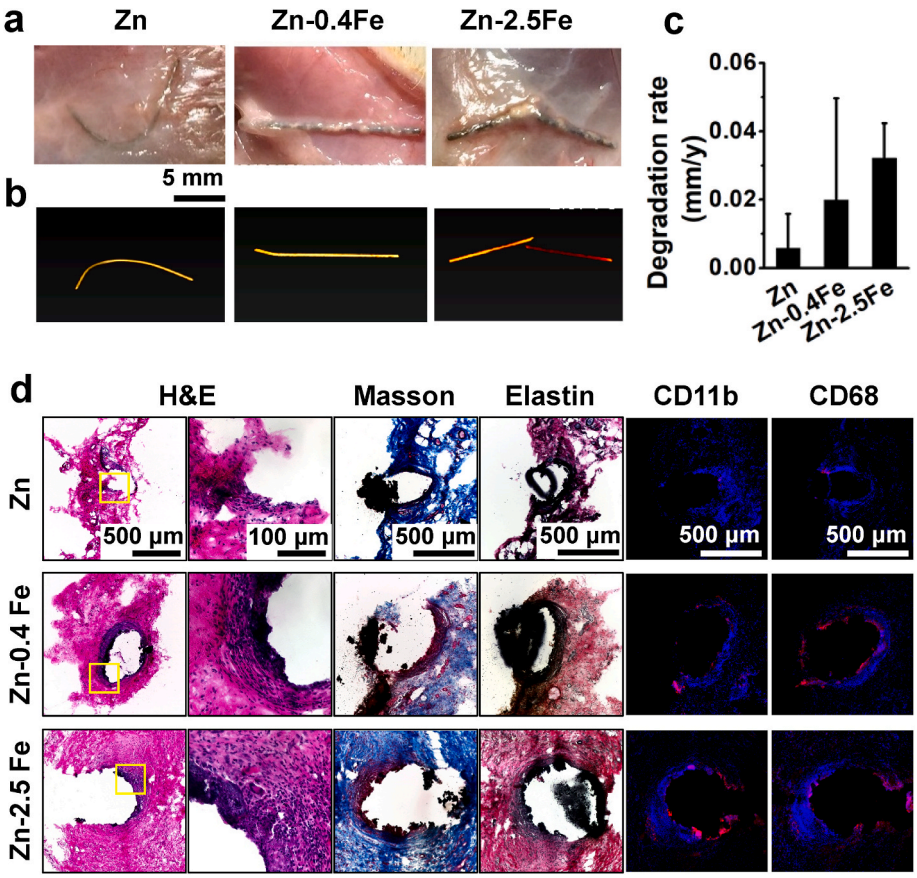

Fig. 6. (a) Macroscopic views, (b) micro-CT scanning images, and (c) degradation rates, and (d) H&E, Masson, elastin, and immunofluorescent staining (CD11b and CD68) of wire implants after implantation with rat subcutaneous tissue for 3 months.

3.6. *In vivo femoral implantation*

Zn and Zn–Fe alloys were next implanted in bone tissue, i.e., the rat femur, to test the degradation behaviors and tissue responses, as shown in Fig. 7 and Fig. 8. The micro-CT scanning images showed the different surface morphology after degradation (Fig. 7a), but the weight loss of all implants was similar with slightly higher values for Zn–Fe alloys (Fig. 7b). The cross-sectional SEM images and EDS mapping in Fig. 7c–f and histological staining images in Fig. 8 showed more detailed information on the degradation products and tissue responses in the implants/tissue interface. The different gray scales in the SEM images are closely related to the elemental compositions in EDS mapping, corresponding to the different tissues and implants in the histological staining images. The little Ca and P content in the EDS mapping (Fig. 7c), the brick red color in Masson-Goldner staining, and the corresponding light red color in Elastin staining (Fig. 8) indicated the formation of osteoid tissue, which is the unmineralized bone matrix that forms prior to the mature bone [41,42].

All implants had similar elemental compositions, bone area percentages, and osteoid tissue formation surrounding the Zn implants (Fig. 7 d and f, Fig. 8). Zn-0.4Fe alloy owned the loosen degradation products and deeper corrosion in the cross sections, and its significantly higher bone-implant contact ratio (BIC) indicated its better bone integration (Fig. 7e). Although the Zn-2.5Fe alloy also had a thick degradation product layer and similar osteoid layer thickness, the osteoid layer did cover most of the implant surface and thus decreased the BIC values significantly.

4. Discussion

In exploring of various biomedical applications (e.g., surgical suture, orthopedic plates and screws), alloying elements (Mg, Ca, Sr, Li, Mn, Cu, and Ag) has been added into Zn materials to improve the mechanical properties [8]. In the present study, two Zn–Fe alloys were fabricated with different microstructures and mechanical property. Mechanical property is closely related to the microstructure of metallic materials. The stiff and fine $FeZn_{15}$ phase uniformly distributed in the Zn matrix significantly strengthened the extruded Zn-0.4Fe alloy while simultaneously increasing the ductility (Fig. 1c). Although the further addition of Fe in Zn-2.5Fe alloy could keep similar mechanical strength, but the ductility decreased significantly due to the dominant amount of the stiff $FeZn_{15}$ phase. Moreover, the cleavage fracture pattern of pure Zn and Zn-2.5Fe alloy (Fig. 1d) could induce a sudden failure of the materials and thus not optimal for the load-bearing applications.

The degradation behavior could influence the mechanical stability of biodegradable materials during the implantation. Zn materials potentially own the most suitable degradation rate for many biomedical applications [2,21], but the localized degradation of pure Zn was harmful for its mechanical integrity in practical service [3–5]. The different phase composition in the alloys after Fe addition changed the degradation patterns. The fine $FeZn_{15}$ phase in Zn-0.4Fe alloy was helpful to form a thin passive film during the long-term degradation, while the dominant amount of $FeZn_{15}$ phase in Zn-2.5Fe alloy promoted the formation of loosen packed degradation products and thus exhibited a more localized degradation pattern than pure Zn and Zn-0.4Fe alloy. The uniform degradation pattern of Zn-0.4Fe alloy in this study was beneficial to maintain sufficient mechanical integrity and long-enough implantation service life (Fig. 2).

It needs to be noted that the degradation behavior is closely related to the micro-environments, e.g., corrosive media and implantation sites [4,43,44]. Compared to the *in vitro* corrosion rates of around 0.6 and 0.05 mm/year from electrochemical and immersion tests (3 month),

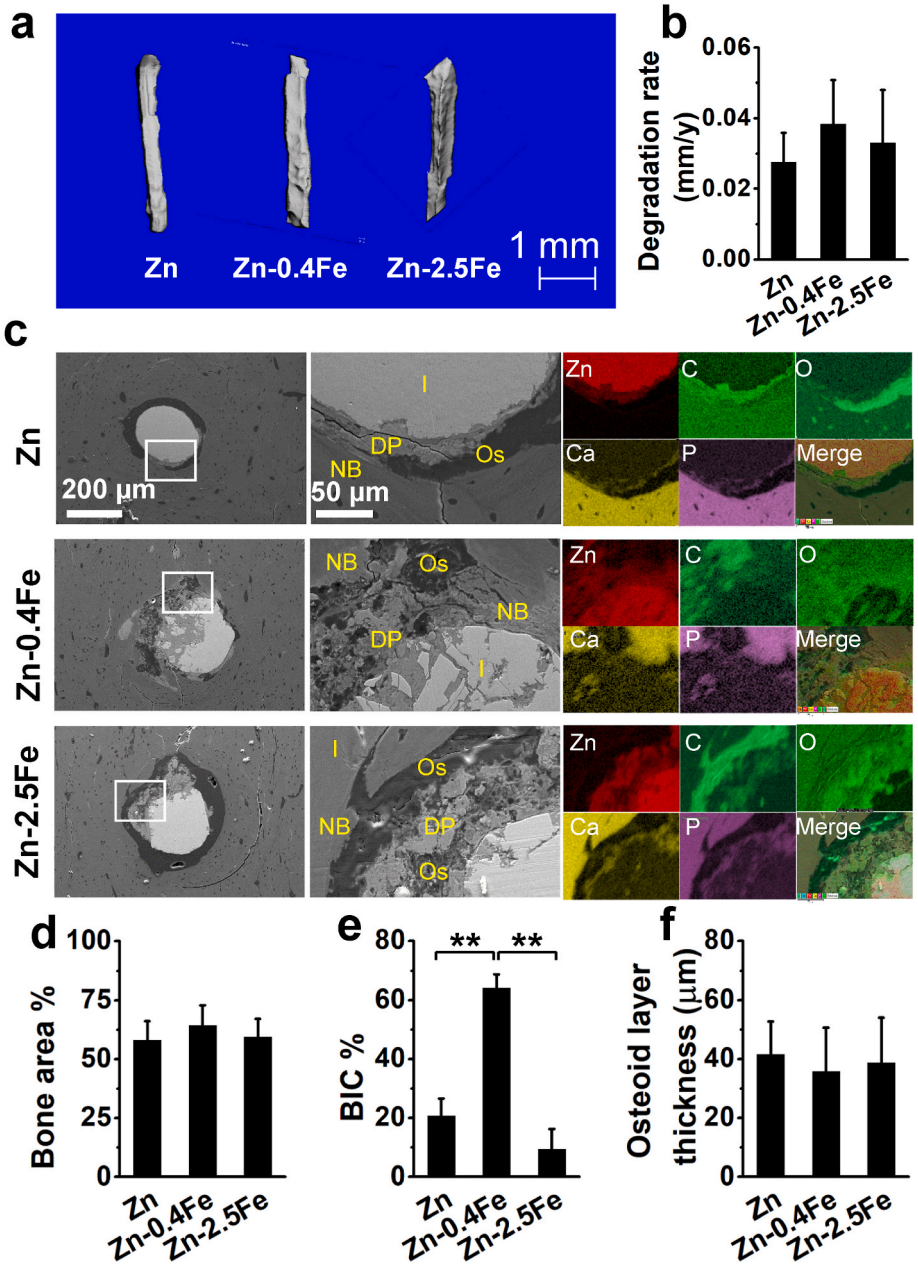

Fig. 7. *In vivo* degradation and bone formation of pure Zn and Zn–Fe alloys when implantation with femoral tissue for 3 months. (a) Micro CT scanning images, (b) degradation rates, (c) cross-sectional SEM images and EDS mapping, (d) new bone area, (e) bone-implant contact ratio (BIC), and (f) osteoid layer thickness surrounding the implants. I: implants, DP: degradation products, OS: osteoid layer, NB: newborn bone.

respectively (Figs. 2c and 3c), the *in vivo* degradation rates decreased to 0.005–0.04 mm/year in both subcutaneous and femoral tissue (Figs. 6c and 7b). Although the Zn and Zn–Fe alloys showed quite comparable corrosion rate *in vitro*, but the *in vivo* degradation of Zn were slowed down, especially in the subcutaneous tissue. The *in vivo* circulation could be one of the main reasons. The active osteoid and new bone formation in the implant/tissue interface could possibly accelerate the body fluid circulation and thus showed corrosive micro-environment and corrosion rates closer to the *in vitro* immersion test.

All Zn materials in this study exhibited good cytocompatibility to the endothelial cells and antiadhesion and antiproliferation abilities to the smooth muscle cells and platelets (Fig. 4). The optimal performances of Zn-0.4Fe alloy is mainly related to its more uniform degradation behavior and the resulted stable interface. The cell viability of endothelial and smooth muscle cells slightly decreased with increasing culture time for all the groups (Fig. 4 d-e). This indicates the concentration levels of Zn ions in the extract media were slightly higher than the tolerance limit of both cells, although the endothelial cells have shown a higher tolerance limit to Zn ions when compared to other cells in our previous studies [8,39,43]. Compared to *in vitro* cytocompatibility, *in vivo* implantation could directly show the host and tissue response to the Zn materials. There was subcutaneous fibrotic encapsulation around all the Zn materials, but the initial stronger macrophage activity from Zn–Fe alloys could be beneficial for the in immunoregulatory and pro-healing process (Fig. 5). Similar to the fibrotic encapsulation formation, the osteoid layer also appeared in the femoral implantation. The degradation products from Zn–Fe alloy could break the coverage of the osteoid tissue layer and thus were mixed with the osteoid tissue (Fig. 7c). The osteoid tissue could be mineralized to new-formed bone tissue using the high content of Ca and P in the degradation products. The uniform degradation behavior of Zn-0.4Fe alloy could be a favor to this biomineralization process and therefore induced a higher bone integration.

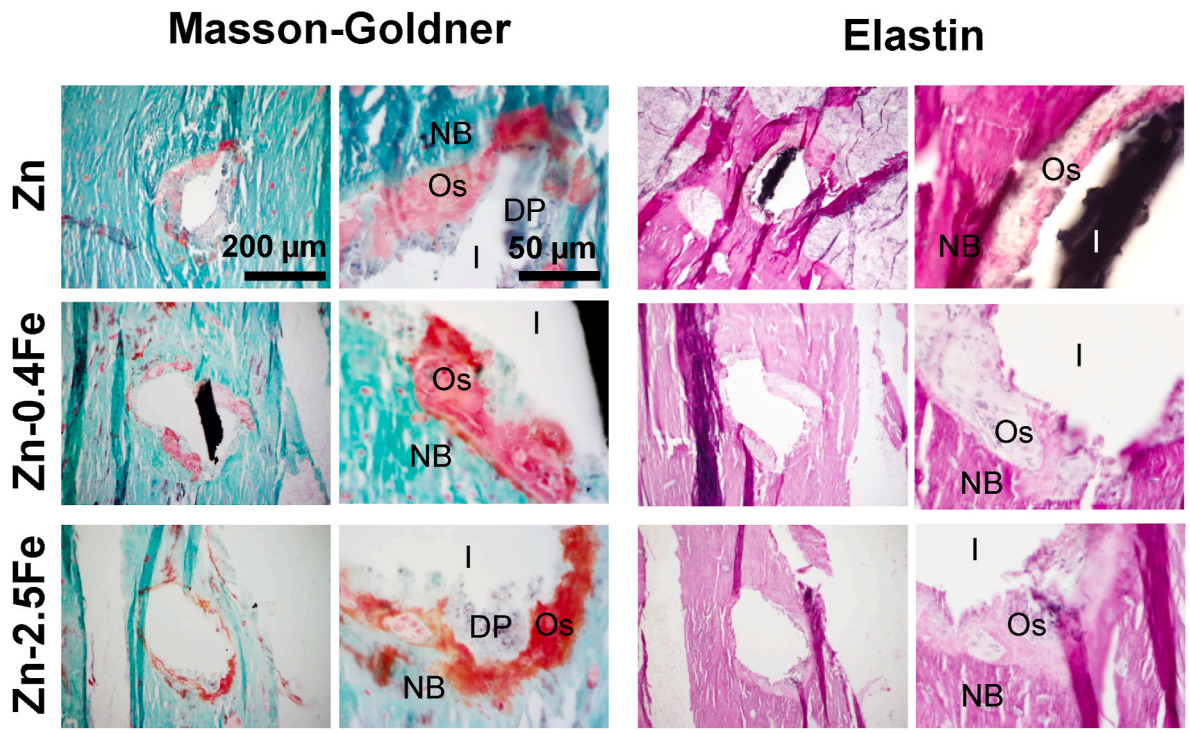

Fig. 8. Masson-Goldner and Elastica van Gieson staining of rat femoral tissue with pure Zn and Zn–Fe alloy wire implantation for 3 months. I: implants, DP: degradation products, OS: osteoid layer, NB: newborn bone.

Antibacterial property is an additional benefit for the Zn based implants due to the outstanding antibacterial potential of Zn ions [9,39,45]. As described in our previous comparable antibacterial study on pure Zn and stainless-steel materials, both bacteria stains could easily aggregate to form a thick biofilm on the stainless-steel surface [5]. There was greatly less bacterial adhesion on the surfaces of pure Zn and Zn–Fe alloys compared to the stainless steel. This indicated that the two Zn–Fe alloys could successfully prevent the biofilm formation of the two bacterial stains we tested. The pH value of bacterial culture media is normally lower than the normal cell media, so the degradation rates in the bacterial culture media would be accelerated and thus the degraded surfaces were quite similar for three Zn materials (Fig. 4). In addition, the different structure and higher sensitivity of *S. aureus* to the Zn ions facilitate the much higher antibacterial rate for *S. aureus* than that for *E. coli* [46].

5. Conclusions

The proposed Zn–Fe alloys in this study possessed different microstructures, which were proven to be the determining factor for the mechanical and degradation properties, and thus significantly influenced their biocompatibility. The stiff and fine $FeZn_{15}$ phase uniformly distributed in the Zn-0.4Fe alloy provided an optical combination of mechanical strength and ductility together with a uniform degradation behavior. Although all Zn materials exhibited similar corrosion rates, *in vitro* cell adhesion, and *in vivo* fibrotic encapsulation and osteoid formation, Zn-0.4Fe alloy exhibited better hemocompatibility and *in vivo* osteointegration. Taken together, the proposed Zn-0.4Fe alloy could be a promising candidate for the load-bearing and other biomedical applications.

CRediT authorship contribution statement

Yingchao Su: Investigation, Data curation, Writing – original draft. **Jiayin Fu:** Subcutaneous implantation investigation, Data curation. **Wonsae Lee:** Femoral implantation investigation. **Shaokang Du:** Alloying and microstructure investigation. **Yi-Xian Qin:** Resources, Writing – review & editing. **Yufeng Zheng:** Resources, Writing – review & editing. **Yadong Wang:** Resources, Writing – review & editing. **Donghui Zhu:** Resources, Writing – review & editing, Supervision.

Declaration of competing interest

All authors declare that they have no conflict of interest.

Acknowledgment

This work was supported by the National Institutes of Health [R01HL140562].

References

[1] Y.F. Zheng, X.N. Gu, F. Witte, Biodegradable metals, Mater. Sci. Eng. R Rep. 77 (2014) 1–34.
[2] P.K. Bowen, E.R. Shearier, S. Zhao, R.J. Guillory 2nd, F. Zhao, J. Goldman, J. W. Drelich, Biodegradable metals for cardiovascular stents: from clinical concerns to recent Zn-alloys, Adv Healthc Mater 5 (10) (2016) 1121–1140.
[3] P.K. Bowen, J. Drelich, J. Goldman, Zinc exhibits ideal physiological corrosion behavior for bioabsorbable stents, Adv. Mater. 25 (18) (2013) 2577–2582.
[4] H. Yang, C. Wang, C. Liu, H. Chen, Y. Wu, J. Han, Z. Jia, W. Lin, D. Zhang, W. Li, W. Yuan, H. Guo, H. Li, G. Yang, D. Kong, D. Zhu, K. Takashima, L. Ruan, J. Nie, X. Li, Y. Zheng, Evolution of the degradation mechanism of pure zinc stent in the one-year study of rabbit abdominal aorta model, Biomaterials 145 (2017) 92–105.
[5] J. Fu, Y. Su, Y.-X. Qin, Y. Zheng, Y. Wang, D. Zhu, Evolution of metallic cardiovascular stent materials: a comparative study among stainless steel, magnesium and zinc, Biomaterials 230 (2020) 119641.
[6] H.F. Li, X.H. Xie, Y.F. Zheng, Y. Cong, F.Y. Zhou, K.J. Qiu, X. Wang, S.H. Chen, L. Huang, L. Tian, L. Qin, Development of biodegradable Zn-1X binary alloys with nutrient alloying elements Mg, Ca and Sr, Sci. Rep. 5 (2015) 10719.
[7] H. Yang, X. Qu, W. Lin, C. Wang, D. Zhu, K. Dai, Y. Zheng, *In vitro* and *in vivo* studies on zinc-hydroxyapatite composites as novel biodegradable metal matrix composite for orthopedic applications, Acta Biomater. 71 (2018) 200–214.
[8] H. Yang, B. Jia, Z. Zhang, X. Qu, G. Li, W. Lin, D. Zhu, K. Dai, Y. Zheng, Alloying design of biodegradable zinc as promising bone implants for load-bearing applications, Nat. Commun. 11 (1) (2020) 401.
[9] Y. Su, I. Cockerill, Y. Wang, Y.X. Qin, L. Chang, Y. Zheng, D. Zhu, Zinc-based biomaterials for regeneration and therapy, Trends Biotechnol. 37 (4) (2019) 428–441.

[10] Y. Liu, Y. Zheng, X.-H. Chen, J.-A. Yang, H. Pan, D. Chen, L. Wang, J. Zhang, D. Zhu, S. Wu, K.W.K. Yeung, R.-C. Zeng, Y. Han, S. Guan, Fundamental theory of biodegradable metals-definition, criteria, and design, Adv. Funct. Mater. 29 (2019) 1805402.
[11] C. Shen, X. Liu, B. Fan, P. Lan, F. Zhou, X. Li, H. Wang, X. Xiao, L. Li, S. Zhao, Mechanical properties, *in vitro* degradation behavior, hemocompatibility and cytotoxicity evaluation of Zn-1.2 Mg alloy for biodegradable implants, RSC Adv. 6 (89) (2016) 86410–86419.
[12] H. Gong, K. Wang, R. Strich, J.G. Zhou, *In vitro* biodegradation behavior, mechanical properties, and cytotoxicity of biodegradable Zn-Mg alloy, J. Biomed. Mater. Res. B Appl. Biomater. 103 (8) (2015) 1632–1640.
[13] N.S. Murni, M.S. Dambatta, S.K. Yeap, G.R.A. Froemming, H. Hermawan, Cytotoxicity evaluation of biodegradable Zn-3Mg alloy toward normal human osteoblast cells, Mater Sci Eng C Mater Biol Appl 49 (2015) 560–566.
[14] M.M. Alves, T. Prošek, C.F. Santos, M.F. Montemor, Evolution of the *in vitro* degradation of Zn–Mg alloys under simulated physiological conditions, RSC Adv. 7 (45) (2017) 28224–28233.
[15] N. Abbaspour, R. Hurrell, R. Kelishadi, Review on iron and its importance for human health, J. Res. Med. Sci.: the official journal of Isfahan University of Medical Sciences 19 (2) (2014) 164.
[16] Z. Yang, Z. Zhang, J. Zhang, Electrodeposition of decorative and protective Zn–Fe coating onto low-carbon steel substrate, Surf. Coating. Technol. 200 (16–17) (2006) 4810–4815.
[17] A. Marder, The metallurgy of zinc-coated steel, Prog. Mater. Sci. 45 (3) (2000) 191–271.
[18] A. Kafri, S. Ovadia, J. Goldman, J. Drelich, E. Aghion, The suitability of Zn–1.3%Fe alloy as a biodegradable implant, Material, Metals 8 (3) (2018) 153.
[19] A. Kafri, S. Ovadia, G. Yosafovich-Doitch, E. Aghion, *In vivo* performances of pure Zn and Zn-Fe alloy as biodegradable implants, J. Mater. Sci. Mater. Med. 29 (7) (2018) 94.
[20] K. Han, I. Ohnuma, K. Okuda, R. Kainuma, Experimental determination of phase diagram in the Zn-Fe binary system, J. Alloys Compd. 737 (2018) 490–504.
[21] J.M. Seitz, M. Durisin, J. Goldman, J.W. Drelich, Recent advances in biodegradable metals for medical sutures: a critical review, Adv Healthc Mater 4 (13) (2015) 1915–1936.
[22] J. Venezuela, M.S. Dargusch, The influence of alloying and fabrication techniques on the mechanical properties, biodegradability and biocompatibility of zinc: a comprehensive review, Acta Biomater. 87 (2019) 1–40.
[23] G. Li, H. Yang, Y. Zheng, X.H. Chen, J.A. Yang, D. Zhu, L. Ruan, K. Takashima, Challenges in the use of zinc and its alloys as biodegradable metals: perspective from biomechanical compatibility, Acta Biomater. 97 (2019) 23–45.
[24] A.J. Drelich, P.K. Bowen, L. LaLonde, J. Goldman, J.W. Drelich, Importance of oxide film in endovascular biodegradable zinc stents, Surface Innovations 4 (3) (2016) 133–140.
[25] A.A.S.f. Testing, Materials, Standard Test Methods for Tension Testing of Metallic Materials, ASTM international, 2009.
[26] J. Levesque, H. Hermawan, D. Dube, D. Mantovani, Design of a pseudo-physiological test bench specific to the development of biodegradable metallic biomaterials, Acta Biomater. 4 (2) (2008) 284–295.
[27] Y. Su, S. Champagne, A. Trenggono, R. Tolouei, D. Mantovani, H. Hermawan, Development and characterization of silver containing calcium phosphate coatings on pure iron foam intended for bone scaffold applications, Mater. Des. 148 (2018) 124–134.
[28] Z.M. Shi, A. Atrens, An innovative specimen configuration for the study of Mg corrosion, Corrosion Sci. 53 (1) (2011) 226–246.
[29] Y. Su, G. Li, J. Lian, A chemical conversion hydroxyapatite coating on AZ60 magnesium alloy and its electrochemical corrosion behaviour, Int. J. Electrochem. Sci. 7 (11) (2012) 11497–11511.
[30] Y. Su, Y. Guo, Z. Huang, Z. Zhang, G. Li, J. Lian, L. Ren, Preparation and corrosion behaviors of calcium phosphate conversion coating on magnesium alloy, Surf. Coating. Technol. 307 (2016) 99–108.
[31] A. G31-12a, Standard Guide for Laboratory Immersion Corrosion Testing of Metals, ASTM West, Conshohocken, PA, 2012.
[32] X. Gu, Y. Zheng, Y. Cheng, S. Zhong, T. Xi, *In vitro* corrosion and biocompatibility of binary magnesium alloys, Biomaterials 30 (4) (2009) 484–498.
[33] S. Hauser, F. Jung, J. Pietzsch, Human endothelial cell models in biomaterial research, Trends Biotechnol. 35 (3) (2017) 265–277.
[34] Y. Wei, F. Chen, T. Zhang, D. Chen, X. Jia, J. Wang, W. Guo, J. Chen, A tubing-free microfluidic wound healing assay enabling the quantification of vascular smooth muscle cell migration, Sci. Rep. 5 (2015) 14049.
[35] J. Lv, L. Wang, J. Zhang, R. Lin, L. Wang, W. Sun, H. Wu, S. Xin, Long noncoding RNA H19-derived miR-675 aggravates restenosis by targeting PTEN, Biochem. Biophys. Res. Commun. 497 (4) (2018) 1154–1161.
[36] J. Ma, N. Zhao, D. Zhu, Endothelial cellular responses to biodegradable metal zinc, ACS Biomater. Sci. Eng. 1 (11) (2015) 1174–1182.
[37] J. Ma, N. Zhao, D. Zhu, Biphasic responses of human vascular smooth muscle cells to magnesium ion, J. Biomed. Mater. Res. 104 (2) (2016) 347–356.
[38] D.A. Robinson, R.W. Griffith, D. Shechtman, R.B. Evans, M.G. Conzemius, *In vitro* antibacterial properties of magnesium metal against Escherichia coli, Pseudomonas aeruginosa and Staphylococcus aureus, Acta Biomater. 6 (5) (2010) 1869–1877.
[39] Y. Su, K. Wang, J. Gao, Y. Yang, Y.X. Qin, Y. Zheng, D. Zhu, Enhanced cytocompatibility and antibacterial property of zinc phosphate coating on biodegradable zinc materials, Acta Biomater. 98 (2019) 174–185.
[40] Y. Jang, Z. Tan, C. Jurey, Z. Xu, Z. Dong, B. Collins, Y. Yun, J. Sankar, Understanding corrosion behavior of Mg–Zn–Ca alloys from subcutaneous mouse model: effect of Zn element concentration and plasma electrolytic oxidation, Mater. Sci. Eng. C 48 (2015) 28–40.
[41] N. Fratzl-Zelman, I. Schmidt, P. Roschger, A. Roschger, F.H. Glorieux, K. Klaushofer, W. Wagermaier, F. Rauch, P. Fratzl, Unique micro-and nano-scale mineralization pattern of human osteogenesis imperfecta type VI bone, Bone 73 (2015) 233–241.
[42] F.H. Glorieux, L.M. Ward, F. Rauch, L. Lalic, P.J. Roughley, R. Travers, Osteogenesis imperfecta type VI: a form of brittle bone disease with a mineralization defect, J. Bone Miner. Res. 17 (1) (2002) 30–38.
[43] Y. Su, H. Yang, J. Gao, Y.X. Qin, Y. Zheng, D. Zhu, Interfacial zinc phosphate is the key to controlling biocompatibility of metallic zinc implants, Adv. Sci. 6 (14) (2019) 1900112.
[44] J. Gao, Y. Su, Y.-X. Qin, Calcium phosphate coatings enhance biocompatibility and degradation resistance of magnesium alloy: correlating *in vitro* and *in vivo* studies, Bioactive Materials 6 (5) (2021) 1223–1229.
[45] Y.W. Wang, A. Cao, Y. Jiang, X. Zhang, J.H. Liu, Y. Liu, H. Wang, Superior antibacterial activity of zinc oxide/graphene oxide composites originating from high zinc concentration localized around bacteria, ACS Appl. Mater. Interfaces 6 (4) (2014) 2791–2798.
[46] Q.L. Feng, J. Wu, G. Chen, F. Cui, T. Kim, J. Kim, A mechanistic study of the antibacterial effect of silver ions on Escherichia coli and Staphylococcus aureus, J. Biomed. Mater. Res. 52 (4) (2000) 662–668.